Journal of
Materials Chemistry C

ROYAL SOCIETY
OF CHEMISTRY

PAPER

View Article Online
View Journal | View Issue

Check for updates

Cite this: *J. Mater. Chem. C*, 2023, **11**, 2345

Rational design of a flexible inorganic composite membrane with an interconnected porous structure as a high-performance lithium ion capacitor electrode†

Xingsheng Li,‡[a] Zhen-Hao Yin,‡[b] Yue Hou,[ac] Chengri Yin[a] and Zhenxing Yin *[a]

Received 22nd October 2022,
Accepted 12th January 2023

DOI: 10.1039/d2tc04482j

rsc.li/materials-c

High-performance lithium-ion capacitors (LICs) have received great attention as a promising power source in the field of portable and wearable electronic devices. However, research on high energy-storage properties and flexibility of LIC electrodes is scarce. Herein, we proposed a novel flexible Cu_xONW/graphene/AgNW (CGA) composite membrane with a uniformly interconnected porous structure for LIC electrodes. Without destroying the CuNW/GO/AgNW membrane structure, the synergism of multiple components (Cu, Cu_2O, and CuO) in the Cu_xONWs and the bonding strength between the three materials can be accurately controlled to achieve a high-performance energy storage electrode. The symmetrical solid-state supercapacitor (SSS) based on CGA-225 membranes exhibited good flexibility (a bending radius of 10 mm) and remarkable electrochemical performance. The LIC assembled with prelithiated CGA-225 presented a large potential window (1–4.5 V), high energy density/power density (maximum, 166 W h kg^{-1}/3,747 W kg^{-1}), and excellent cycling stability (92.6% of the initial capacitance after 10 000 cycles at 20 mA cm^{-2}).

Introduction

The rapid development of portable and wearable electronic devices towards miniaturization and integration has dramatically increased human demand for high-performance energy storage devices in modern society.[1–4] Lithium-ion capacitors (LICs) are considered to be one of the ideal candidates for energy storage, due to their high energy density, high power density, long cycle life, fast charge–discharge rate, and safety.[5–7] To meet the higher growing requirements of human beings for portable and wearable electronic devices, recently, the flexibility of LICs has been often explored by scientific and technological researchers. However, it is difficult for the current LIC electrodes to have both high-energy storage performance and flexibility.

Conventional LIC electrodes are usually coated with powder-type materials on 2D planar collectors, and their structures are more easily broken during the charging/discharging or mechanical deformation, leading to a capacitance attenuation.[8–11] In order to improve the energy-storage performance and flexibility of electrodes, many researchers began to construct nanocomposite membrane electrodes[12–15] composed of one-dimensional metal oxides and two-dimensional carbon materials, because of their remarkable advantages arising from the unique structure and material properties.[16–21] For instance, Deng *et al.* fabricated a LIC by using Nb_2O_5 nanorod/carbon cloth as an anode and activated carbon (AC) as a cathode, which had a maximum gravimetric energy density (95.55 W h kg^{-1} at 191 W kg^{-1}) and a good reversibility (a bend angle in the range of 30° to 180°).[22] Huo *et al.* reported that the LIC assembled with an AC/CNT/rGO cathode and a $Li_4Ti_5O_{12}$ nanorod/CNT/rGO anode exhibited a high energy density of 67 W h kg^{-1} at 1589 W kg^{-1} and a capacitance retention rate of 60.4% at 0.2 C after 1000 cycles.[23] Meanwhile, the flexible $Li_4Ti_5O_{12}$ nanorod/CNT/rGO film anode is very suitable for wearable electronic devices. However, these composite membrane electrodes are still not competitive in the current LIC due to their relatively low capacitance.

Recently, copper-based oxides (Cu_2O and CuO) that have the advantages of low cost, abundant reserves, and high specific capacitance are a promising electrode material for LICs.[24–27] Unfortunately, their nanomaterials are prone to aggregation caused by large surface energy, which significantly hinders the electron migration rate. It is worth noting that a very effective strategy is to use graphene with excellent structural properties[28–32] as a scaffold to improve the dispersion of copper-based oxide nanomaterials, thereby enhancing the conductivity and flexibility

---

[a] *Department of Chemistry, National Demonstration Centre for Experimental Chemistry Education, Yanbian University, Yanji, Jilin 133002, China. E-mail: yinzx@ybu.edu.cn*

[b] *Department of Environmental Science, Yanbian University, Yanji, Jilin 133002, China*

[c] *Yanbian Zhenxing Electronic Technology Co., Ltd., Yanji, Jilin 133000, China*

† Electronic supplementary information (ESI) available. See DOI: **https://doi.org/10.1039/d2tc04482j**

‡ These authors have contributed equally to this work.

of the composite membrane. Due to the presence of oxygen-containing functional groups on the graphene surface and the high contact resistance at the junctions, the overall conductivity of copper-based oxide/graphene nanocomposites is far from meeting the requirements of the practical application in high-performance flexible LICs. Therefore, it is necessary to introduce highly conductive metal nanomaterials (such as Ag nanowires (NWs)) into this system to improve the internal electron migration capability of composite membrane electrodes.[33]

Herein, we successfully produced a novel flexible Cu_xONW/graphene/AgNW (CGA) composite membrane with a uniformly interconnected porous structure through simple vacuum filtration and air annealing. When the original membrane morphology is not destroyed, the oxidation of CuNWs to Cu_xONWs, the reduction of graphene oxide (GO) to graphene, and the tight bonding of the three materials (Cu_xONWs, graphene nanosheets, and AgNWs) are simultaneously achieved during the annealing process. In the CGA composites, the synergistic effect of multiple components (Cu, Cu_2O, and CuO) in Cu_xONWs plays a very important role in the enhancement of electrode capacitance. The symmetrical solid-state supercapacitor (SSS) composed of two flexible CGA membranes showed high electrochemical performance and good flexibility. In addition, the LICs with a prelithiated CGA-225 membrane anode exhibited a large operating potential range, high energy density, high power density, and excellent cycle stability. The developed thin-membrane CGA electrode has extensive application prospects in the fields of electrocatalysis and flexible energy storage devices.

Experimental section

Preparation of CuNWs

The CuNWs were synthesized by using our previously reported method.[34] CuCl (3 mmol), NH_4Cl (0.45 mmol), and oleylamine (9 mmol) were dissolved in a polyol solution that contained 30 mL ethylene glycol (EG), 20 mL glycerol (GC), and 10 mL polyethylene $glycol_{200}$. Then, the mixed solution was heated to 110 °C under vigorous stirring and held at this temperature for 20 min to form a Cu(I)–amine complex. Finally, the reaction temperature was heated to 200 °C at a heating rate of 10 °C min^{-1} and the mixture refluxed for 20 min. The reaction solution was quickly quenched with cold water for 5 min, and washed with *n*-hexane and isopropanol (IPA) three times. The obtained CuNWs were dispersed in IPA to prepare a composite membrane electrode.

Preparation of a Cu_xONW/graphene/AgNW (CGA) membrane

The AgNWs were synthesized according to the method reported in the literature.[35] The CGA membrane was prepared by vacuum filtration and air annealing. Graphite oxide[36] was dissolved in IPA and treated in an ultrasonic bath for 2 h to form a 1 mg mL^{-1} graphene oxide (GO) solution. The CuNW/IPA dispersion (45 mL, 1 mg mL^{-1}) and AgNW/IPA dispersion (45 mL, 3 mg mL^{-1}) were sequentially added to 45 mL of GO solution under continuous magnetic stirring. Afterwards, a homogeneous solution was obtained through sonication of the ternary mixture solution for 1 h. Immediately afterwards, the obtained dispersion was subjected to vacuum filtration with a cellulose acetate (CA) membrane (0.2 μm pore size and 47 μm diameter; Advantec) to prepare a CuNW/GO/AgNW membrane. Wherein the materials in all composite membranes had the same mass ratio (CuNWs : GO : AgNWs = 1 : 1 : 3, w : w : w). The membrane was easily peeled off from the CA membrane with a knife and dried overnight at room temperature. Finally, the as-prepared CuNW/GO/AgNW was annealed at 225 °C for 2 h under an air atmosphere to obtain monolithic CGA. For the ease of presentation, the CGA at different temperatures for 2 h was denoted as CGA-X, where X is 150 °C, 175 °C, 200 °C, 225 °C, 250 °C, 275 °C, and 300 °C, respectively. For example, the annealing CGA at 225 °C is denoted as CGA-225.

Characterization

The crystal structure, microscopic morphology, and chemical composition of the prepared samples were analyzed by X-ray diffractometry (XRD, Bruker, D8 DISCOVER), scanning electron microscopy (FESEM, Hitachi, SU8010), transmission electron microscopy (TEM, JEOL JEM-2100Plus), Raman spectroscopy (512 nm laser source, Horiba, LabRAM HR Evolution), and X-ray photoelectron spectroscopy (XPS, Shimadzu, ESCA 3400). Thermogravimetric analysis (TGA) was carried out by using a PerkinElmer TGA7/DSC7 analyzer heated from 25 to 800 °C in air at a rate of 5 °C min^{-1}. The membrane thickness was measured using a spiral micrometer. Measurements of electrical conductivity were obtained using a Digital Source-Meter with four probes (Keithley, 2461).

Electrochemical measurements

The 2032 coin-type half-cell lithium-ion battery (LIB) and full-cell lithium-ion capacitor (LIC) were assembled in an argon atmosphere glove box. The best CGA-225 (active material, graphene and Cu_xO, 3 ± 0.2 mg) membrane was cut into 12 mm diameter discs, and then directly used as the electrode of LIBs and LICs. The half-cell LIB consisted of a CGA-225 working electrode, Celgard 2500 separator, $LiPF_6$ electrolyte, and Li sheet counter electrode. The anode prelithification process was realized by the sacrificed electrode method. An AC cathode was prepared by coating slurry onto the Al foil. The full-cell LIC consists of a prelithified CGA-225 anode and commercial AC cathode. To balance the capacitance of the anode and cathode, the optimal mass ratio of CGA-225 and AC is 1 : 2.5. The electrochemical performance was carried out on a CHI660E electrochemical workstation (Shanghai Chenhua, China). The cycling performance test of half-cell LIBs was performed on a CT2001A tester (Wuhan LAND, China). The areal capacitance (C_A) and specific capacitance (C_s) of the prepared membranes were calculated from the GCD curves:

$$C_A = \frac{I \times \Delta t}{\Delta U \times S}$$

$$C_s = \frac{I \times \Delta t}{\Delta U \times V}$$

where I (mA) is the discharge current, Δt (s) is the discharge time, S (cm^2) is the area of the working electrode, m (g) is the mass of the active material of the working electrode, and ΔU (V) is the discharge potential window. The specific energy (E, W h kg^{-1}) and specific power (P, W kg^{-1}) of the LICs were calculated as:

$$E = \frac{1}{2} C_s \Delta U^2$$

$$P = \frac{E}{\Delta t}$$

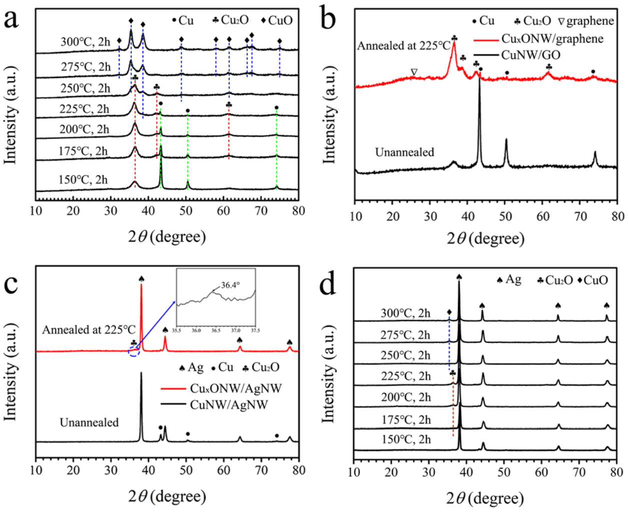

Fig. 1 XRD patterns of (a) the oxidation of the CuNW membrane at different annealing temperatures for 2 h, (b) CuNW/GO and Cu$_x$ONW/graphene, (c) CuNW/AgNW and Cu$_x$ONW/AgNW, and (d) CGA composite membrane at different annealing temperatures for 2 h.

Results and discussion

The fabrication process of the CGA composite membrane is shown in Scheme 1. Firstly, we use pre-synthesized active materials (GO and CuNWs) and a highly conductive current collector (AgNWs) to construct the CuNW/GO/AgNW precursors of flexible electrodes with uniformly interconnected porous structures by controllable and low-cost physical methods (ultrasound, dynamic stirring, and vacuum filtration). Subsequently, the precursor membrane was placed in a tube furnace and annealed *in situ* to prepare a high-performance flexible CGA composite membrane. The oxidation of CuNWs to Cu$_x$ONWs and the reduction of GO to graphene occurred simultaneously during this air annealing process, which did not damage the initial membrane structure. Importantly, the phase component of the Cu$_x$ONWs in the CGA can be precisely controlled by adjusting the annealing temperature and time. The prepared CGA membranes can be directly used as electrodes of SSS (CGA-225//CGA-225) and LIC (CGA-225//AC) without any conductive agents, adhesives, current collector foil, and further processing.

The phase and crystallinity of the as-prepared membranes were studied using X-ray diffraction (XRD) patterns. In order to explore the fine structural changes of the CuNWs in the CGA during the oxidation process, a series of experiments were carried out at different annealing temperatures (150–300 °C) for 2 h. As shown in Fig. 1a and Fig. S1a (ESI†), besides the characteristic peaks of Cu, the CuNW membrane annealed at 150 °C also exhibited three weak peaks at 2θ = 36.4°, 42.3°, and 61.3° corresponding to the (111), (200), and (220) planes of Cu$_2$O (JCPDS #05-0667), respectively.[37] It is proved that CuNWs are partially oxidized to Cu$_2$ONWs. As we all know, oxygen diffuses from the surface to the inside during the oxidation of metals. Increasing reaction temperature and extending reaction time can improve the oxidation rate of metals. When the temperature increased from 150 °C to 225 °C, the characteristic peak intensity of the Cu$_2$ONWs increased, while the characteristic peak intensity of the CuNWs decreased. Significantly, the peak intensity decreased at 225 °C, which may be attributed to the formation of a small amount of CuO. When the temperature is increased to 300 °C, all the characteristic peaks of the samples at 2θ = 32.5°, 35.5°, 38.7°, 48.7°, 58.3°, 61.5°, 66.2°,

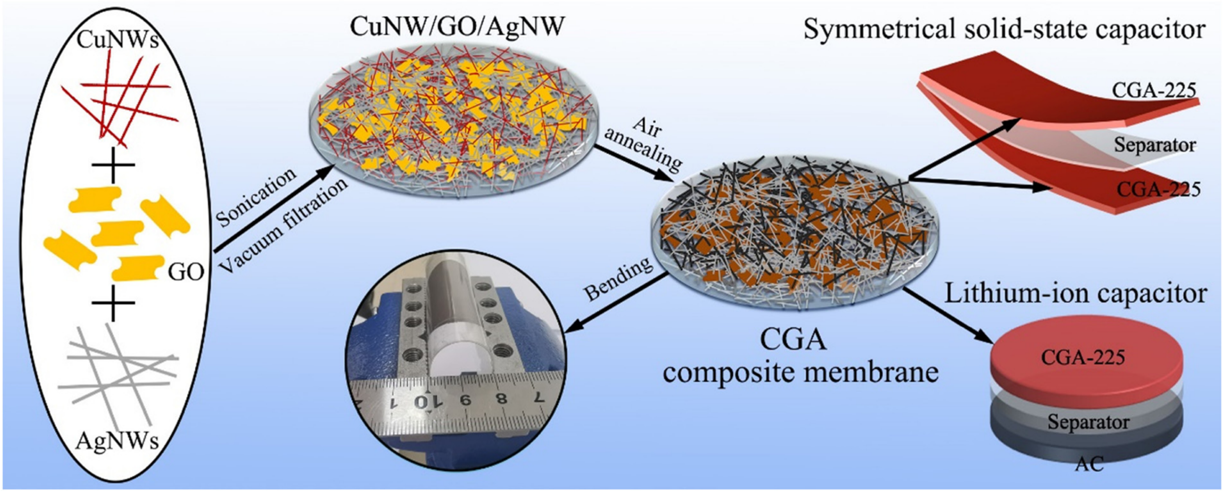

Scheme 1 The fabrication process of the CGA composite membrane, symmetric solid-state supercapacitor, and lithium-ion capacitors.

67.9°, and 74.9° were assigned to the (110), (11-1), (111), (20-2), (202), (11-3), (31-1), (113), and (004) planes of CuO (JCPDS #48-1578), respectively, indicating that CuNWs were completely oxidized to CuONWs. The Cu_xONW/graphene showed a broad peak (26°) and a strong peak (36.4°) in Fig. 1b, which demonstrated that GO was reduced to graphene and Cu was oxidized to Cu_2O during the air annealing process. After annealing at 225 °C for 2 h, the GO/AgNW was transformed into graphene/AgNW (Fig. S1b, ESI†), and the CuNW/AgNW was transformed into Cu_xONW/AgNW (Fig. 1c). Furthermore, the characteristic peaks of Ag and Cu_2O (36.4°) were observed, while those of Cu and CuO were not observed due to the strong Ag signal coverage. Interestingly, the oxidation process of the CuNW/GO/AgNW was similar to that of CuNWs. With an increase of reaction temperature, furthermore, the intensities of all characteristic peaks in CGA-225 increased, which meant that the crystallinity of Ag and Cu_2O improved (Fig. 1d). Based on the above analysis, CGA-225 was composed of Ag, graphene, Cu_2O, Cu, and CuO.

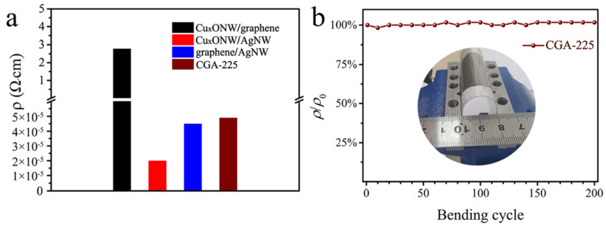

Fig. 2 (a) Resistivity of Cu_xONW/graphene, graphene/AgNW, Cu_xONW/AgNW, and CGA-225. (b) Resistivity change of CGA-225 after 200 cycles (bending radius: 10 mm).

The resistivity (ρ) of the membrane was further systematically measured to evaluate its electrical properties. As shown in Fig. 2a, Cu_xONW/graphene exhibited a relatively high resistivity (2.3 Ω cm), which might lead to a decrease in the capacitance of LICs. In order to improve the electrochemical performance of Cu_xONW/graphene, it is essential to introduce highly conductive AgNWs. After adding AgNWs, the resistivity changes of these composite membranes were further studied in Fig. 2a. The resistivity of the Cu_xONW/AgNW (2.0×10^{-5} Ω cm), graphene/AgNW (4.5×10^{-5} Ω cm), and CGA-225 (4.9×10^{-5} Ω cm) was much smaller than that of the Cu_xONW/graphene, because of the high electron mobility of AgNWs in the linear direction. It can be seen that the presence of two-dimensional graphene nanosheets significantly increased the contact points with one-dimensional NWs, thereby enhancing the contact resistance. As a result, the resistivity of graphene/AgNW and CGA-225 was more than 2 times that of the Cu_xONW/AgNW. In the course of the experiment, moreover, it was surprising to find that CGA-225 not only had excellent electrical conductivity and electrochemical performance, but also had an outstanding flexibility. Based on the comprehensive consideration, we, hence, selected CGA-225 as a research object to further test the mechanical stability. Due to the highly stable graphene–AgNW skeleton, the resistivity change (ρ/ρ_0) of CGA-225 was negligible after 200 bends at a bending radius of 10 mm (Fig. 2b), indicating its high flexibility and high structural stability, which is very suitable for flexible LIC electrodes.

The surface morphology evolution of CuNW/GO/AgNW before and after air annealing was studied by SEM, as shown in Fig. 3. In Fig. 3a, CuNWs (less than 100 nm in diameter) were

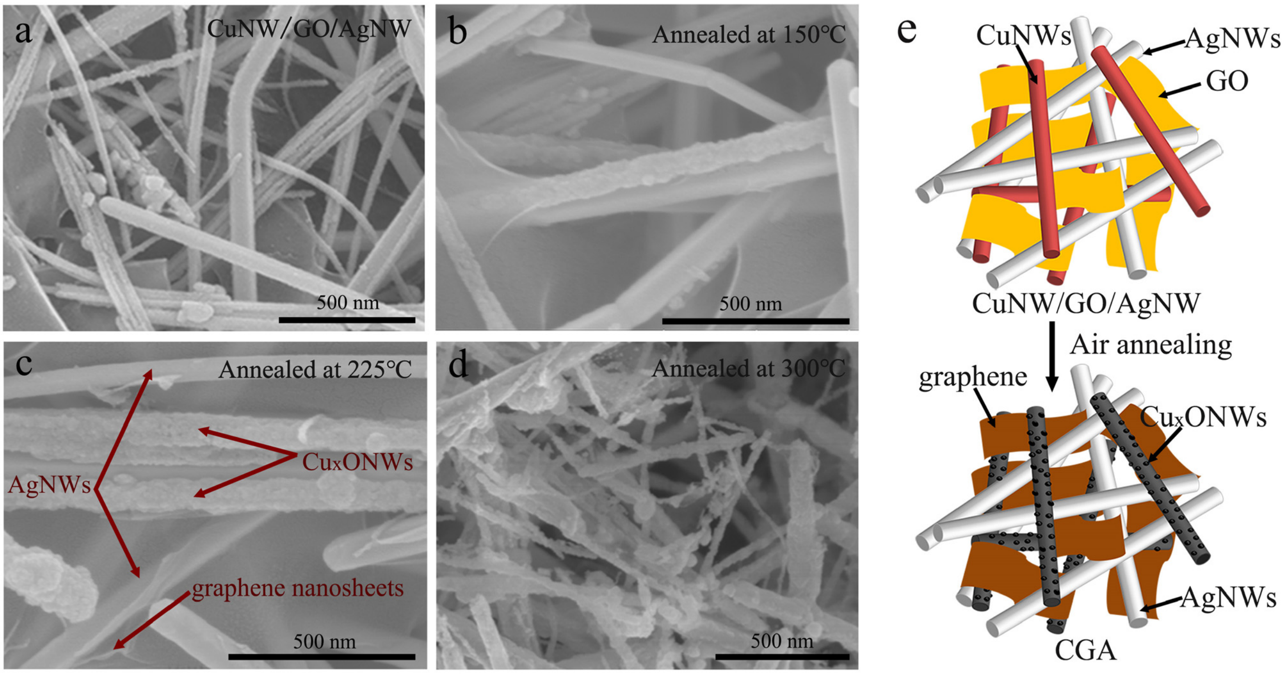

Fig. 3 SEM images of (a) CuNW/GO/AgNW, (b) CGA-150, (c) CGA-225, and (d) CGA-300. (e) Schematic diagram of the structural change from CuNW/GO/AgNW to CGA.

uniformly loaded on the GO nanosheets, forming a uniformly interconnected porous membrane. After annealing at 150 °C for 2 h, the CuNWs in CGA-150 were partially transformed into Cu_xONWs with protruding particles on the surface, whereas GO nanosheets were partly reduced to graphene nanosheets. Thus, CGA-150 mostly maintained the initial structure (Fig. 3a and b). Compared with CGA-150, the morphology of CGA-225 remained unchanged, and the Cu_xONWs with protruding particles were slightly increased in diameter after annealing at 225 °C (Fig. 3c and Fig. S2, ESI†). Notably, the initial structure was perfectly maintained after annealing, which was beneficial to improve mechanical and electrochemical properties. Interestingly, when the temperature increased from 150 °C to 225 °C, the crystallinity of Cu_2O (Fig. 1) and the size of the protruding particles on the Cu_xONW surface increased simultaneously. When annealed at 300 °C, the Cu component was completely oxidized to CuO, as proven in the XRD result (Fig. 1). Fig. 3d shows the NW morphology in the membrane after annealing at 300 °C. It is clearly seen that the CuONW diameter increased slightly without fracture; however, the AgNW structure was broken and transformed into short nanorods, which was caused by exceeding its heat deflection temperature.

The effect of reaction time on the CGA-225 morphology was further studied. With the increase of the annealing time, the morphology of CGA-225 showed almost no change, but the content and crystallinity of the Cu_2ONWs gradually increased (Fig. S3 and S4, ESI†). Therefore, it can be seen that the CuNWs are transformed into multi-component Cu_xONWs with an increase in annealing temperature and time, which reduces the CGA flexibility. Based on the above experimental results, it can be concluded that 225 °C and 2 h were the optimal preparation conditions for the CGA membrane with the best flexibility and electrochemical performance. For better understanding of the structural changes from CuNW/GO/AgNW to CGA, we used a schematic diagram to illustrate the reaction (Fig. 3e). During air annealing at 225 °C for 2 h, the AgNW morphology was not changed due to their high stability at low temperatures. According to the principle of thermal reduction and metal oxidation, the oxygen-containing functional groups on the GO nanosheet surface fell off and were reduced to graphene nanosheets, while the CuNWs were oxidized to Cu_xONWs with protruding particles on the surface. To determine the content of each component in the CuNW/GO/AgNW membrane, we carried out TGA analysis of GO/AgNW and CuNW/GO. As shown in Fig. S5 (ESI†), the GO was completely burned after air calcination, while GO/AgNW and CuNW/GO were converted into Ag_2O and CuO, respectively. It can be inferred that the mass ratio of GO and Ag in GO/AgNW was about 1 : 3, while that of Cu and GO in CuNW/GO was about 1 : 1. Based on the thermogravimetric analysis of GO/AgNW and CuNW/GO, the mass ratio of Cu, GO, and Ag in CuNW/GO/AgNW was approximately 1 : 1 : 3.

The chemical composition of CGA-225 was further characterized using XPS. As shown in Fig. 4a, the peaks at 284.5, 368.2, 532.0, and 932.2 eV corresponded to the spectra of C1s, Ag3d, O1s, and Cu2p, respectively, which proved that CGA-225 contained graphene, Ag, Cu, Cu_2O, and CuO. Compared with CuNW/GO/AgNW, the intensity of C and Cu of CGA-225 increased while the intensity of O decreased (Fig. S6, ESI†), indicating the reduction of graphene and the oxidation of Cu. The existence of Ag3d (368.2 eV and 374.2 eV) showed that Ag was not oxidized at 225 °C in air (Fig. S7a, ESI†),[38] which is consistent with the XRD results. Furthermore, the difference in oxidation temperature between the AgNWs and the CuNWs could be explained by the second law of thermodynamics. Because the standard Gibbs free energy of formation of Cu was lower than that of Ag, there was an obvious oxidation temperature gap between Cu and Ag under the same conditions. Therefore, the CuNWs were oxidized to Cu_2ONWs and AgNWs were not oxidized at 225 °C for 2 h in air (Fig. 4 and Fig. S7a, ESI†), which is fully consistent with previous XRD results (Fig. 1d). The C1s spectrum in Fig. 4b showed that peaks at 284.6, 286.6, and 288.3 eV were attributed to C–C, C═O, and C–O, respectively, demonstrating the reduction of GO to graphene. To further evaluate the reduction degree of graphene, we used the intensity ratio (I_D/I_G) of the D band and G band of the Raman spectrum to semi-quantitatively analyze CGA-225. As shown in Fig. S7b (ESI†), the intensity ratio of CGA-225 (1.13) is significantly greater than that of CuNW/GO/AgNW (0.99), which implies an increase in the degree of disorder and graphitization of graphene after annealing. The core spectra of Cu2p (Fig. 4c) contained three peaks of Cu^+ (932.2, 952.2 eV), Cu^0 (932.55, 952.55 eV), and Cu^{2+} (934.6, 953.7 eV),[39] indicating that the Cu_xO in CGA-225 comprised of Cu, Cu_2O and CuO. Additionally, the O1s peak (Cu–O, 529.4 eV) in Fig. 4d further confirmed the existence of Cu_2O. To investigate the effect of Cu_xO in CGA composite membranes on the electrochemical properties, we used the high-resolution Cu2p XPS spectra to analyze the ratio of each component. Fig. S8 and Table S1 (ESI†) show that the atomic percentage ratios (at%) of Cu^+, Cu^0, and Cu^{2+} for CGA-150, CGA-225 and CGA-300 were 56.5 : 43.5 : 0, 90.4 : 3.9 : 5.7, and 0 : 0 : 100, respectively. It can be seen that the annealing temperature and time play a key role in the component proportion and crystallinity of Cu_xO (Cu, Cu_2O,

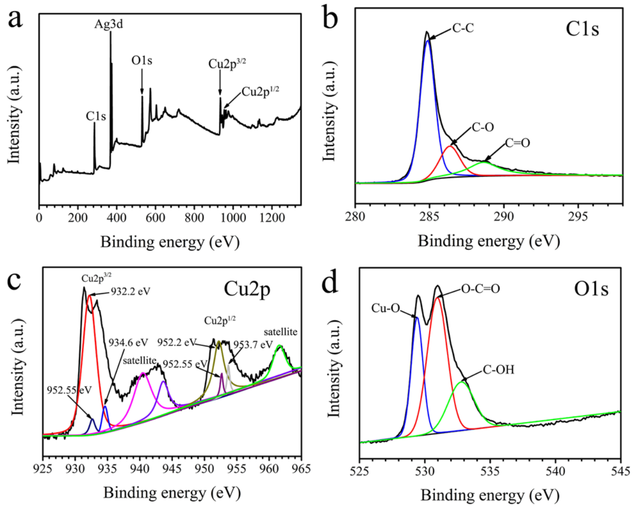

Fig. 4 XPS spectra of (a) survey spectrum, (b) C 1s, (c) Cu 2p, and (d) O 1s of CGA-225.

and CuO), thereby improving the electrochemical performance of the CGA.

The electrochemical performance of the prepared membrane electrode was tested in the standard three-electrode system using 1 M KOH aqueous solution as electrolyte. To achieve the optimum electrochemical performance, the areal capacitance of CGA at different annealing temperatures was systematically tested (Fig. 5a). As the annealing temperature increased from 150 °C to 225 °C, the areal capacitance of CGA gradually increased at the same current density, which was caused by the conversion of CuNWs into Cu_2ONWs and the reduction of GO to graphene. Meanwhile, the protruding structures on the Cu_x-ONW surface and the bonding between Cu, Cu_2O, and CuO respectively increased the active sites and electron mobility, thereby improving the electrochemical performance of the electrode. When the annealing temperature was increased from 225 °C to 275 °C, the areal capacitance of CGA gradually decreased, which was attributed to the partial conversion of Cu and Cu_2O to CuO in the Cu_xONWs. At 300 °C, CGA-300 had the smallest areal capacitance because of the structural destruction of the AgNWs and the disappearance of Cu. It is generally known that CuO has a higher theoretical specific capacitance and poor cycle stability, while Cu_2O has the opposite performance. In particular, the lifetime is a very important parameter for the practical application of the electrode, so we chose Cu_xO (Cu–Cu_2O–CuO) NWs with structural stability as the main research object. In Cu_xONWs, the Cu_2O plays a major role in the capacitive contribution. The results showed that the CGA annealed at 225 °C had the largest areal capacitance. At the same annealing temperature of 225 °C, we further tested the effect of time on the areal capacitance of the CGA (Fig. 5b). With an extension of the reaction time, the capacitance of CGA showed a trend of first increasing and then decreasing, and the capacitance was the largest when the reaction time was 2 h. These results suggested that the oxidation degree of Cu and the reduction degree of graphene played a decisive role in improving the electrode capacitance.

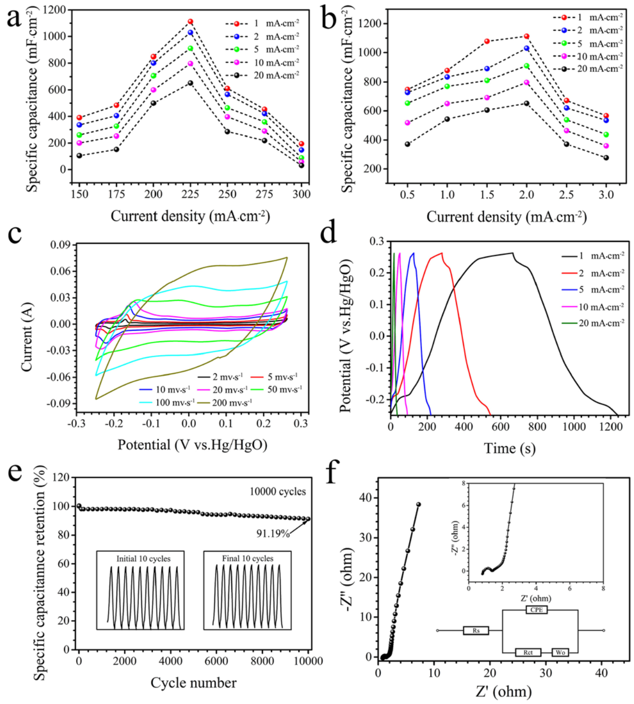

Fig. 5 (a) Areal capacitance of CGA at different annealing temperatures for 2 h at different current densities. (b) Areal capacitance of CGA-225 annealed at 225 °C for different time at different current densities. (c) CV curves of CGA-225 at different scan rates. (d) CV curves of CGA-225 at different current densities. (e) Cycle stability of CGA-225 at a current density of 10 mA cm^{-2}. (f) Nyquist plot of CGA-225. Inset: Enlarged diagram of high-frequency area and equivalent circuit diagram.

Fig. S7a (ESI†) shows the areal capacitance of CGA-225 membranes with different thicknesses, which can be adjusted by increasing the amount of the mixture. At a current density of 1 mA cm^{-2}, as the mass of the active materials increased, the areal capacitance of CGA-225 was in the order 150 μm (563.3 mF cm^{-2}) < 310 μm (1,113.4 mF cm^{-2}) < 460 μm (1,482.4 mF cm^{-2}). During the experiment, we found that the limit bending radii of 150 μm, 310 μm, and 460 μm of the CGA-225 membranes were 5 mm, 8 mm and 25 mm, respectively. If the bending radius of the membrane exceeded the limit, the structure was easy to be broken. Currently, the bending radius of the flexible supercapacitors tends to exceed 10 mm, and the bending limit (5 mm and 8 mm) of CGA-225 (150 μm and 310 μm) is better than the common standard. To balance the bending and electrochemical performance, a 310-μm membrane was selected as the optimal electrode of the flexible supercapacitor.

Fig. 5c shows the CV curves of CGA-225 from -0.249 to 0.263 V *vs.* Hg/HgO at different scan rates from 2 to 200 mV s^{-1}. The CV curves of CGA-225 presented a quasi-rectangular shape due to the electric double layer capacitance (EDLC) characteristics of graphene. In addition, a pair of redox peaks were clearly observed around −0.21 V and −0.17 V in the CV curves, which was related to the redox reaction of Cu_2O in 1 M KOH solution. The possible faradaic redox reactions are expressed as:

$$Cu_2O + 2OH^- = 2CuO + H_2O + 2e^- \quad (1)$$

$$Cu_2O + H_2O + 2OH^- = 2Cu(OH)_2 + 2e^- \quad (2)$$

In the whole redox reactions, the oxidation peak represented the transformation of Cu_2O to CuO and $Cu(OH)_2$, and the reduction peak indicated the conversion of CuO and $Cu(OH)_2$ to Cu_2O. These results indicated that the CGA electrode had both EDLC (graphene) and pseudocapacitance (copper-based oxide) characteristics. Furthermore, with the increase of the scan rates, the redox peak gradually disappeared, indicating that the primary electrode reaction changed from diffusion control to surface reaction control.

The areal capacitance of CGA-225 was calculated according to the GCD curves in Fig. 5d. The areal capacitance of the CGA-225 membrane was 1,113.4, 1,030.1, 911.2, 796.9, and 652.3 mF cm^{-2} at 1, 2, 5, 10, and 20 mA cm^{-2}, respectively, showing a high specific capacitance and a good rate performance. In comparison, the capacitance of CGA-225 in Fig. S7b (ESI†) was significantly higher than that of Cu_xO/AgNW (820.3 mF cm^{-2}), graphene/

AgNW (623.3 mF cm^{-2}), and Cu$_x$ONW/graphene (19.1 mF cm^{-2}). Based on the above comparison, the superior electrochemical performance of CGA-225 was attributed to the collective effect of AgNWs with excellent conductivity and Cu$_x$ONW/graphene nanocomposites with high capacitance that is better than that of graphene-based and copper-based oxide electrodes reported in other literature studies (Table S2, ESI†). In Fig. 5e, CGA-225 exhibited an excellent cycle stability (~91.2% of the initial capacitance) after 10 000 charge–discharge cycles at a current density of 10 mA cm^{-2}. The Nyquist plot was used to analyze the resistance of CGA-225 between 0.01 Hz and 10 kHz, as shown in Fig. 5f. The solution resistance R_s (the intercept of the real axis) and the charge-transfer resistance R_{ct} (the diameter of the flat semicircle) were only 0.9 Ω and 0.5 Ω, respectively. According to physical and electrochemical characterization, the annealing temperature and time can accurately adjust the phase component and morphology of Cu$_x$ONWs and the reduction degree of graphene nanosheets, thereby improving the electrochemical performance of the CGA membranes.

The excellent electrochemical performance of CGA-225 is mainly due to the following advantages: (1) the protruding particles on the Cu$_x$ONW surface with the synergistic effect of multiple components (Cu, Cu$_2$O, and CuO) could increase the redox-active sites; (2) the highly stable graphene–AgNW skeleton could effectively buffer the structural expansion of Cu$_x$ONWs during the charge–discharge process, thereby improving the cycle stability of the CGA membrane electrode; and (3) the uniformly interconnected porous structure could increase the contact area of the electrolyte ions and shorten the electron migration path.

To be closer to practical applications, we investigated the electrochemical performance of SSS and LICs assembled with the best performing CGA-225 membrane electrode. The prepared membrane can be directly used as a free-standing and binder-free electrode of a SSS without further processing. Compared with the three-electrode system, the CV curves of the SSS (1 × 1 cm^2) in Fig. 6a had a quasi-rectangular shape without redox peaks, indicating that the charging and discharging were carried out at a pseudo-constant rate.[44] In Fig. 6b, the areal capacitance of the SSS was 480.2, 445.7, 390.6, 308.6, and 210.9 mF cm^{-2} at 1, 2, 5, 10, and 20 mA cm^{-2}, respectively, showing a high specific capacitance and a good rate performance. Remarkably, the SSS in Fig. 6c had good cycle stability (~88.6% of the initial capacitance) after 5000 charge–discharge cycles. The good electrochemical performance of the SSS may be mainly ascribed to the tight interface contact of the interconnected porous structure of the CGA-225 membranes with the KOH/PVA gel electrolyte, which effectively promotes the role of active materials and improves the structure stability of the electrode. The illustration in Fig. 6c showed that the R_s and R_{ct} values of the SSS had increased tinily, which proved that the electrode structure was only slightly damaged.

A flexible electronic device usually requires a certain degree of flexibility in the power supply device. Therefore, we tested the bending performance of a SSS (2 × 4 cm^2) at a bending radius of 10 mm. At a current density of 10 mA cm^{-2}, the SSS still maintained 80.7% of the initial capacitance (Fig. 6d), and its R_{ct} value increased from 0.6 Ω to 33.4 Ω after 2,000 bending cycles (inset of Fig. 6d), suggesting that the perfect combination of the porous CGA-225 membrane with high structural stability and PVA/KOH gel electrolyte can effectively relieve the stress in the long-term charge–discharge process and mechanical deformation, so that the SSS exhibits good flexibility and high cycling stability. The test results show that the CGA-225 composite membrane is an ideal electrode for flexible SSSs.

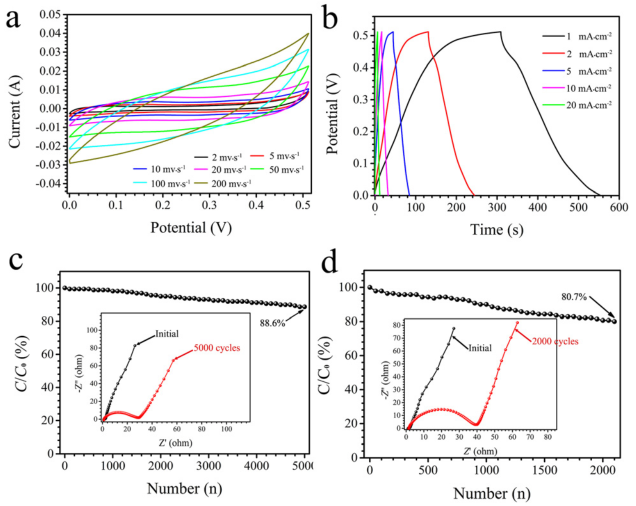

Fig. 6 The electrochemical performance of a SSS. (a) CV curves at different scan rates, (b) GCD curves at different current densities, and (c) cycle stability curve at 10 mA cm^{-2}. (d) Cyclic stability of the SSS after 2000 bending cycles at a current density of 10 mA cm^{-2}. Inset: Nyquist plots of the SSS.

In order to further investigate the electrochemical performance of CGA-225 in LiPF$_6$ electrolyte, CV and GCD measurements are carried out half-cell with Li sheets as a counter electrode in the potential range of 0.01–3.0 V(*vs.* Li/Li$^+$) at different current densities. Interestingly, the capacity change trend of CGA composite membranes with different annealing temperatures in LiPF$_6$ electrolyte was similar to that of aqueous electrolyte (Fig. S10, ESI†), in which the CGA-225 composite membrane had the best electrochemical performance. The lithiation/delithiation reactions of Cu$_x$O were analyzed by the CV curves at low scan rates, as shown in Fig. 7a. At a scan rate of 0.2 mv s^{-1}, there are three reduction peaks around 2.34, 1.49 and 0.72 V (*vs.* Li/Li$^+$) during the discharging process, which correspond to the conversion of CuO to Cu$_2$O (eqn (3)), the further conversion of Cu$_2$O to Cu (eqn (4)), and the formation of a solid electrolyte interphase (SEI) membrane, respectively. In contrast, the oxidation reaction of the charging process is the reverse reaction of the discharging process.

$$2\text{CuO} + 2\text{Li}^+ + 2\text{e}^- = \text{Cu}_2\text{O} + \text{Li}_2\text{O} \quad (3)$$

$$\text{Cu}_2\text{O} + 2\text{Li}^+ + 2\text{e}^- = 2\text{Cu} + \text{Li}_2\text{O} \quad (4)$$

Furthermore, as the scan rate increases, the redox peak shifts slightly due to electrode polarization. Generally, the charge storage mechanism of materials can be revealed by the power

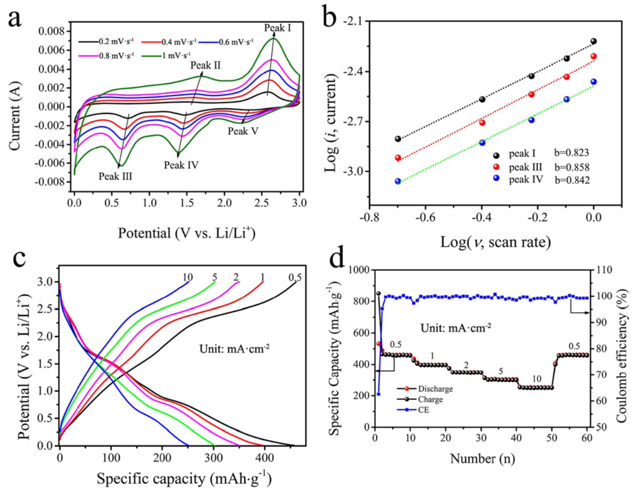

Fig. 7 Electrochemical performances of the CGA-225 membrane electrode in a Li half-cell between 0.01 and 3 V. (a) CV curves at low scan rates. (b) Power law relationship between redox peak current and scan rates. (c) GCD curves and (d) rate performance at different current densities.

law formula $i = a\nu^b$ (or $\log i = b\log\nu + \log a$), where i is the current, ν is the scan rate, and a and b are adjustable parameters. In the logarithmic formula, $b = 0.5$ indicates a semi-infinite linear diffusion process, whereas $b = 1$ indicates a surface-controlled process. In Fig. 7b, the b values of peak I, peak III, and peak IV are 0.823, 0.858, and 0.842, respectively. It shows that the charge storage is mainly dominated by the surface capacitive behavior, and the diffusion of the bulk phase is limited. In Fig. 7c and d, the average specific capacitances of CGA-225 (active materials: ∼3 mg) at 0.5, 1, 2, 5, and 10 mA cm^{-2} were 460, 396, 349, 301, and 251 mA h g^{-1}, respectively, indicating that it had high capacity, excellent cyclic stability, and good rate capability. This is mainly due to the high stability of the composite membrane structure and the collective effect of lithiophilic Cu$_x$ONWs, graphene, and AgNWs. Furthermore, the average specific capacitance of the AC cathode in the potential range of 2–4.5 V was 119.4, 97.2, 86.5, 74.3, and 63.6 mA h g^{-1} at 0.5, 1, 2, 5, and 10 mA cm^{-2}, respectively (Fig. S11, ESI†), showing a good rate performance.

As we all know, the asymmetric electrodes can broaden the potential window of LICs and increase their energy density. Therefore, we construct LICs with a prelithiated CGA-225 anode and a commercialized AC cathode. The working mechanism of the CGA-225//AC LIC is shown in Fig. 8a. During the charge process, Li$^+$ cations are intercalated into graphene sheets and Cu$_x$ONWs of the CGA-225 anode, while PF$_6^-$ anions are rapidly adsorbed onto the AC cathode. The discharge reaction of the electrodes is the reverse reaction of the charging process. The curves of the CGA-225 anode (0.01–3 V) and AC cathode (2–4.5 V) show typical pseudocapacitive and capacitive behaviors, respectively (Fig. 8b). According to the GCD curve, we selected 1–4.5 V as the working voltage range of LICs. To balance the capacity of the anode and cathode in LICs, the optimal mass ratio of CGA-225 (active material: ∼3 mg) and AC is 1 : 2.5. In Fig. 8c, the curves of the CGA-225//AC LIC exhibited pseudocapacitive characteristics due to the coupling effect of the different lithium storage mechanisms of the anode and cathode. The GCD curves of the CGA-225//AC LIC with different current densities are presented in Fig. 8d. At current densities of 2, 5, 10, and 20 mA cm^{-2}, the

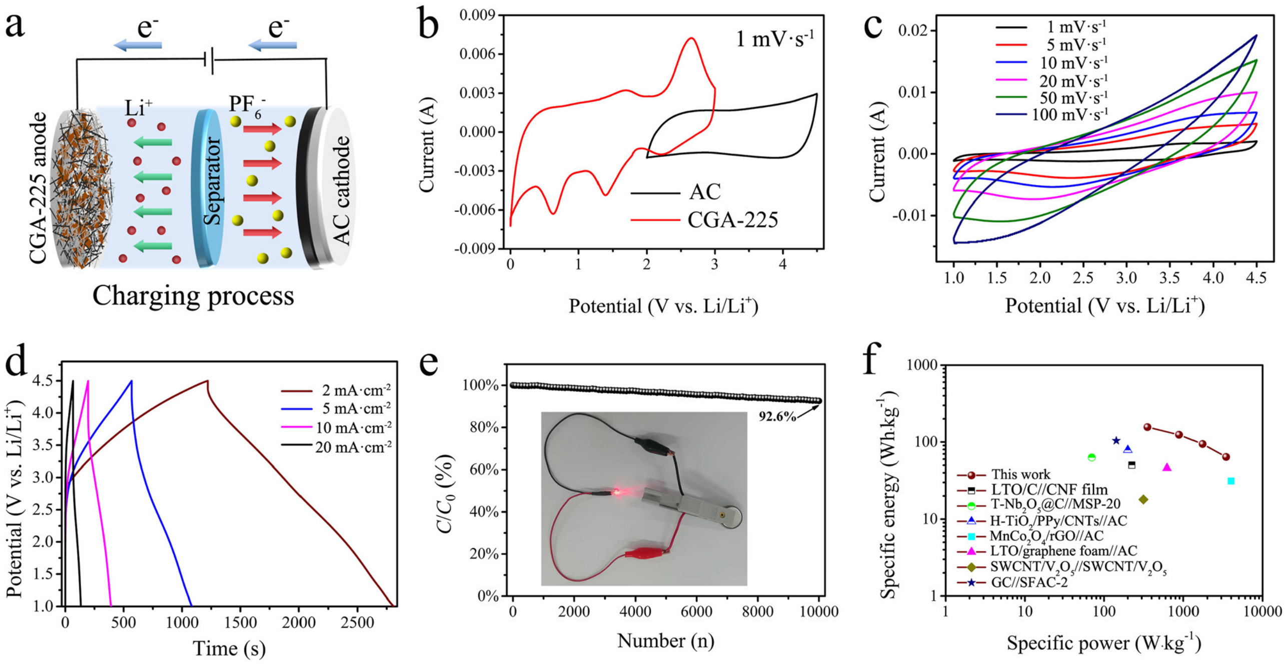

Fig. 8 Electrochemical performance of the CGA-225//AC LIC. (a) Schematic diagram of the reaction mechanism. (b) CV curves of the CGA-225 anode and AC cathode. (c) CV curves at different scan rates. (d) GCD curves at different current densities. (e) Cycling performance at 20 mA cm^{-2}. The inset of e is the LIC device powering the red light-emitting diode (LED). (f) Ragone plots of the CGA-225//AC LIC and previously reported LICs.

CGA-225//AC LIC achieved a high specific capacitance of 97.8, 79.1, 59.9, and 41 F g^{-1}, respectively. The shape of GCD curves is an approximate isosceles triangle, showing good capacitive/pseudocapacitive performance. Moreover, the CGA-225//AC LIC also exhibited excellent cycling stability with 92.6% of the original capacity after 10 000 cycles at 20 mA cm^{-2} (Fig. 8e), showing that the CGA-225 electrode is very suitable for high-rate charge and discharge. In the inset of Fig. 8e, the fabricated LIC device can power a red LED for 1 h, demonstrating its potential for practical application. According to Ragone plots, the fabricated CGA-225//AC LIC delivered high energy densities of 166, 135, 102, and 70 W h kg^{-1} at power densities of 378, 945, 1,882, and 3,747 W kg^{-1}, respectively. Notably, the energy densities and power densities of the CGA-225//AC LIC are better than those of most of the previously reported LICs (Fig. 8f).[40–46]

The excellent electrochemical performance of LICs is attributed to the following factors. Highly conductive and lithiophilic porous structures facilitate the rapid reciprocating transport of electrons and electrolyte ions (Li^+ and PF_6^-) and suppress the generation of lithium dendrites. The tight connections between each composition are beneficial to the improvement of the electrochemical performance of Cu_xONWs and graphene sheets. More importantly, the coexistence of multiple components in Cu_xO (Cu, Cu_2O, and CuO) NWs greatly enhances the pseudocapacitance of LICs. The perfect coupling of the CGA-225 cell-type anode with high reaction kinetics and the AC capacitive-type cathode with fast adsorption capability can enhance the rate capability of LICs.

Conclusions

In summary, we successfully prepared a novel flexible Cu_xONW/graphene/AgNW (CGA) composite membrane with an interconnected porous structure using simple vacuum filtration and air annealing. By adjusting the annealing temperature and time, the phase component and morphology of the Cu_xO (Cu, Cu_2O, and CuO) NWs and the bonding strength between the Cu_xONWs, graphene nanosheets, and AgNWs could be precisely controlled to obtain a CGA membrane electrode with both high flexibility and high capacitance. Electrochemical test results showed that the SSS assembled by two flexible CGA-225 composite membrane electrodes and a PVA/KOH gel electrolyte exhibited a high areal capacitance of (480.2 mF cm^{-2}) and good flexibility (80.7%, 2000 cycles, bending radius: 10 mm). The LICs assembled with a prelithiated CGA-225 membrane anode and commercial AC cathode exhibit a large operating potential range (1–4.5 V), high energy density (166 W h kg^{-1} at 378 W kg^{-1}), high power density (3,747 W kg^{-1} at 70 W h kg^{-1}), and excellent cycling stability (92.6% of the initial capacitance after 10 000 cycles at 20 mA cm^{-2}). Also, the developed membrane is expected to be applied in a flexible energy storage device to power small-volume wearable and portable electronic devices.

Conflicts of interest

The authors declare no competing financial interest.

Acknowledgements

This work was supported by the National Natural Science Foundation of China (52163031 and 42061042) and the Department of Science and Technology of Jilin Province (20220403041RC).

References

1 L. Wen, F. Li and H. M. Cheng, *Adv. Mater.*, 2016, **28**, 4306–4337.
2 Y. Liu, X. Zhou, Y. Bai, R. Liu, X. Li, H. Xiao, Y. Wang, X. Wang, Y. Ma and G. Yuan, *Chem. Eng. J.*, 2021, **417**, 127955.
3 Y. S. Wang, S. M. Li, S. T. Hsiao, W. H. Liao, S. Y. Yang, C. C. M. Ma and C. C. Hu, *J. Mater. Chem. C*, 2015, **3**, 4987–4996.
4 J. Liu, W. Peng, Y. Li, F. Zhang and X. Fan, *J. Mater. Chem. C*, 2021, **9**, 6308–6315.
5 S. Dong, H. Li, J. Wang, X. Zhang and X. Ji, *Nano Res.*, 2017, **10**, 4448–4456.
6 Z. Hu, S. Sayed, T. Jiang, X. Zhu, C. Lu, G. Wang, J. Sun, A. Rashid, C. Yan, L. Zhang and Z. Liu, *Adv. Energy Mater.*, 2018, **8**, 1802273.
7 B. Deng, H. Dong, T. Lei, N. Yue, L. Xiao and J. Liu, *Sci. China Mater.*, 2020, **63**, 492–504.
8 A. Jagadale, X. Zhou, R. Xiong, D. P. Dubal, J. Xu and S. Yang, *Energy Storage Mater.*, 2019, **19**, 314–329.
9 M. Soltani and S. H. Beheshti, *J. Energy Storage*, 2021, **34**, 102019.
10 Y. Li, Y. Wang, R. Cai, C. Yu, J. Zhang, J. Wu, C. S. Tiwary, J. Cui, Y. Zhang and Y. Wu, *J. Colloid Interf. Sci.*, 2022, **610**, 385–394.
11 J. T. Su, S. H. Lin, C. C. Cheng, P. Y. Cheng and S. Y. Lu, *J. Power Sources*, 2022, **531**, 231345.
12 H. Kim and P. A. Kohl, *J. Power Sources*, 2010, **195**, 2224–2229.
13 G. Zhou, D. Wang, F. Li, P. Hou, L. Yin, C. Liu, G. Q. Lu, I. R. Gentle and H. Cheng, *Energy Environ. Sci.*, 2012, **5**, 8901–8906.
14 K. Mishra, N. Yadav and S. A. Hashmi, *J. Mater. Chem. A*, 2020, **8**, 22507–22543.
15 Q. Wu, D. Liang, S. Lu, J. Zhang, H. Wang, Y. Xiang and D. Aurbach, *ACS Appl. Mater. Interfaces*, 2021, **13**, 46537–46548.
16 X. Dai, W. Shi, H. Cai, R. Li and G. Yang, *Solid State Sci.*, 2014, **27**, 17–23.
17 B. Chen, Y. Wang, C. Li, L. Fu, X. Liu, Y. Zhu, L. Zhang and Y. Wu, *RSC Adv.*, 2017, **7**, 25019–25024.
18 L. Lyu, K. Seong, D. Ko, J. Choi, C. Lee, T. Hwang, Y. Cho, X. Jin, W. Zhang, H. Pang and Y. Piao, *Mater. Chem. Front.*, 2019, **3**, 2543–2570.
19 Y. Liu, K. Sun, X. Cui, B. Li and J. Jiang, *ACS Sustainable Chem. Eng.*, 2020, **8**, 2981–2989.
20 X. Zhang, Q. Fan, S. Liu, N. Qu, H. Yang, M. Wang and J. Yang, *Inorg. Chem. Front.*, 2020, **7**, 204–211.
21 D. Adekoya, M. Li, M. Hankel, C. Lai, M. S. Balogun, Y. Tong and S. Zhang, *Energy Storage Mater.*, 2020, **25**, 495–501.
22 K. K. Lee, W. S. Chin and C. H. Sow, *J. Mater. Chem. A*, 2014, **2**, 17212–17248.
23 P. Du, Y. Dong, H. Kang, X. Yang, Q. Wang, J. Niu, S. Wang and P. Liu, *ACS Sustainable Chem. Eng.*, 2018, **6**, 14723–14733.

24 C. Dong, Y. Wang, J. Xu, G. Cheng, W. Yang, T. Kou, Z. Zhang and Y. Ding, *J. Mater. Chem. A*, 2014, **2**, 18229–18235.

25 W. Yuan, Z. Qiu, Y. Chen, B. Zhao, M. Liu and Y. Tang, *Electrochim. Acta*, 2018, **267**, 150–160.

26 X. Mao, Y. Zou, F. Xu, L. Sun, H. Chu, H. Zhang, J. Zhang and C. Xiang, *ACS Appl. Mater. Interfaces*, 2021, **13**, 22664–22675.

27 J. Wang, L. Yang, Y. Fu, P. Yin, X. Guan and G. Wang, *Nanoscale*, 2021, **13**, 8562–8574.

28 M. F. El-Kady, Y. Shao and R. B. Kaner, *Nat. Rev. Mater.*, 2016, **1**, 16033.

29 V. D. Nithya, *J. Energy Storage*, 2021, **44**, 103380.

30 Y. Li, X. Wang, Q. Yang, M. S. Javed, Q. Liu, W. Xu, C. Hu and D. Wei, *Electrochim. Acta*, 2017, **234**, 63–70.

31 Y. Murashima, M. R. Karim, R. Furue, T. Matsui, H. Takehira, K. Wakata, K. Toda, R. Ohtani, M. Nakamura and S. Hayami, *Inorg. Chem. Front.*, 2016, **3**, 842–848.

32 Y. Shao, H. Wang, Q. Zhang and Y. Li, *J. Mater. Chem. C*, 2013, **1**, 1245–1251.

33 H. Absike, M. Hajji, H. Labrim, A. Abbassi and H. Ez-Zahraouy, *Superlattices Microstruct.*, 2019, **127**, 128–138.

34 Z. Yin, S. K. Song, S. Cho, D. J. You, J. Yoo, S. T. Chang and Y. S. Kim, *Nano Res.*, 2018, **10**, 3077–3091.

35 S. Jeong, H. Cho, S. Han, P. Won, H. Lee, S. Hong, J. Yeo, J. Kwon and S. H. Ko, *Nano Lett.*, 2017, **17**, 4339–4346.

36 X. Li, Y. Wang, Y. Hou, C. Yin and Z. Yin, *Composites, Part A*, 2021, **140**, 106192.

37 S. Deng, V. Tjoa, H. M. Fan, H. R. Tan, D. C. Sayle, M. Olivo, S. Mhaisalkar, J. Wei and C. H. Sow, *J. Am. Chem. Soc.*, 2012, **134**, 4905–4917.

38 W. J. Liu, M. L. Liu, S. Lin, J. C. Liu, M. Lei, H. Wu, C. Q. Dai and Z. Y. Wei, *Opt. Express*, 2019, **27**, 16440–16448.

39 H. Meng, W. Yang, K. Ding, L. Feng and Y. Guan, *J. Mater. Chem. A*, 2015, **3**, 1174–1181.

40 H. Xu, X. Hun, Y. Sun, W. Luo, C. Chen, Y. Liu and Y. Huang, *Nano Energy*, 2014, **10**, 163–171.

41 E. Lim, C. Jo, H. Kim, M. H. Kim, Y. Mun, J. Chun, Y. Ye, J. Hwang, K. S. Ha, K. C. Roh, K. Kang, S. Yoon and J. Lee, *ACS Nano*, 2015, **9**, 7497–7505.

42 G. Tang, L. Cao, P. Xiao, Y. Zhang and H. Liu, *J. Power Sources*, 2017, **355**, 1–7.

43 L. Q. Fan, J. L. Huang, Y. L. Wang, C. L. Geng, S. J. Sun, Y. F. Huang and J. H. Wu, *J. Energy Storage*, 2020, **30**, 101427.

44 Y. Qian, X. Cai, C. Zhang, H. Jiang, L. Zhou, B. Li and L. Lai, *Electrochim. Acta*, 2017, **258**, 1311–1319.

45 V. Aravindan, Y. L. Cheah, W. F. Mak, G. Wee, B. V. R. Chowdari and S. Madhavi, *ChemPlusChem*, 2012, **77**, 570–575.

46 Z. Yang, H. Guo, X. Li, Z. Wang, J. Wang, Y. Wang, Z. Yan and D. Zhang, *J. Mater. Chem. A*, 2017, **5**, 15302.